



Title	Modeling of light propagation in the human neck for diagnoses of thyroid cancers by diffuse optical tomography
Author(s)	Fujii, H.; Yamada, Y.; Kobayashi, K.; Watanabe, M.; Hoshi, Y.
Citation	International Journal for Numerical Methods in Biomedical Engineering, 33(5), e2826 https://doi.org/10.1002/cnm.2826
Issue Date	2017-05
Doc URL	http://hdl.handle.net/2115/70062
Rights	This is the peer reviewed version of the following article: International Journal for Numerical Methods in Biomedical Engineering 33(5) May 2017 e2826, which has been published in final form at http://onlinelibrary.wiley.com/doi/10.1002/cnm.2826/full . This article may be used for non-commercial purposes in accordance with Wiley Terms and Conditions for Self-Archiving.
Type	article (author version)
File Information	NMBE_Fujii.pdf



[Instructions for use](#)

Modeling of light propagation in the human neck for diagnoses of thyroid cancers by diffuse optical tomography

H. Fujii^{*1}, Y. Yamada², K. Kobayashi¹, M. Watanabe¹, and Y. Hoshi³

¹ *Division of Mechanical and Space Engineering, Faculty of Engineering, Hokkaido University, Kita 13 Nishi 8, Kita-ku, Sapporo, Hokkaido 060-8628, Japan*

² *Brain Science Inspired Life Support Research Center, University of Electro-Communications, 1-5-1 Chofugaoka, Chofu, Tokyo 182-8585, Japan*

³ *Preeminent Medical Photonics Education & Research Center, Hamamatsu University School of Medicine, 1-20-1 Handayama, Higashi-ku, Hamamatsu, Sizuoka 431-3192, Japan*

SUMMARY

Diffuse optical tomography (DOT) using near-infrared light in a wavelength range from 700 nm to 1000 nm has the potential to enable non-invasive diagnoses of thyroid cancers, some of which are difficult to detect by conventional methods such as ultrasound tomography. DOT needs to be based on a physically accurate model of light propagation in the neck, because it reconstructs tomographic images of the optical properties in the human neck by inverse analysis. Our objective here was to investigate the effects of three factors on light propagation in the neck using the 2D time-dependent radiative transfer equation: (i) the presence of the trachea, (ii) the refractive-index mismatch at the trachea-tissue interface, and (iii) the effect of neck organs other than the trachea (spine, spinal cord, and blood vessels). We found that there was a significant influence of reflection and refraction at the trachea-tissue interface on the light intensities in the region between the trachea and the front of the neck surface. Organs other than the trachea showed little effect on the light intensities measured at the front of the neck surface although these organs affected the light intensities locally. These results indicated the necessity of modeling the refractive-index mismatch at the trachea-tissue interface and the possibility of modeling other neck organs simply as a homogeneous medium when the source and detectors were far from large blood vessels. Copyright © 2016 John Wiley & Sons, Ltd.

Received . . .

1. INTRODUCTION

Diffuse optical tomography (DOT), which is still under development, offers great promise for a non-invasive hemodynamic evaluation and cancer detection in a range of organs and tissue, and among these imaging of the thyroid gland by DOT has not been reported. This may be ascribed to ultrasound as the primary modality for assessment of thyroid lesions. However, distinguishing thyroid follicular cancers from follicular adenomas is extremely difficult even with fine needle aspiration. Definitive diagnosis of follicular cancer can be made only by a histological examination of a thyroidectomy specimen: here the essential features for the diagnosis are vascular and/or capsular invasion of tumor cells [1]. It is expected that DOT will be of help here, because DOT has the potential to detect these histopathological features from tomographic images of the optical properties (absorption and scattering coefficients) using near-infrared light in a wavelength range from 700 nm to 1000 nm.

Near-infrared light penetrates deeply into biological tissue with multiple scattering. As a result, only diffused light is detected at the tissue surface in actual measurements. Due to the diffused light propagation, obtaining clear DOT images is not straightforward, unlike X-ray computed tomography. With DOT there is an inversion process involved in reconstructing the tomographic images of the optical properties based on a light propagation model describing the phenomenon of light scattering and absorption [2, 3, 4, 5]. To obtain high quality DOT images, the accuracy in the light propagation model used in the forward problem is critical. As for the measuring method for DOT, there are three types of measurement; continuous wave, frequency-domain, and time-domain measurements [2, 3, 5]. Among them, the time-domain measurement using ultra-short light pulses with a pulse width in the order of picoseconds provides the richest information to obtain

*Correspondence to: H. Fujii, Faculty of Engineering, Hokkaido University, Kita 13 Nishi 8, Kita-ku, Sapporo, Hokkaido Japan.

†E-mail: fujii-hr@eng.hokudai.ac.jp

high quality DOT images. Therefore, in this study, we employ time-domain measurement and solve time-dependent equation for light propagation of ultra-short light pulse.

It is widely accepted that the radiative transfer equation (RTE) is the most accurate deterministic light propagation model, however the numerical calculations with the RTE involve a heavy computational load because it is an integro-differential equation with many independent variables: position, angular direction, and time. Because of this, DOT based on the RTE has been applied to only small tissue volumes such as human fingers [6] and rats [7]. With a larger tissue volume (like the human head), DOT has used diffusion approximation (DA) to reduce computation loads by assuming isotropic scattering. Comparing to DOT based on the RTE, DOT based on the DA has been developed for clinical use [8, 12], and accordingly extensive simulation studies using the DA have justified the feasibility of DOT to detect and quantify primary blast lung [10] and brain injury [11]. Because the DA holds in the diffusive regions in scattering media, it fails to describe light propagation in non-scattering and highly absorbing media [13]. Monte Carlo (MC) simulation is often employed for calculating light propagation in organs and tissue volumes by generating random numbers. The MC simulation, however, requires long computation times to reduce statistical noises. Although some efforts to shorten the computation times have been made [14], the MC method still needs further development to obtain the results with low levels of statistical noises. In this paper, we employ the RTE among the light propagation models.

The human neck is a large and heterogeneous medium with a wide variation of the optical properties, including the thyroid gland, trachea, blood vessels, muscles, bones, adipose tissues, and more. The trachea is a void region where light propagates straight without being absorbed or scattered. Meanwhile, the blood vessels are highly absorbing media, where light is strongly absorbed before it undergoes multiple scattering processes. This makes it impossible to use the DA for the trachea and blood vessels, and numerical calculations of the RTE in the human neck are necessary for prediction of light propagation. In addition, reflection and refraction occur at the trachea boundary and the external boundary of the human neck due to refractive-index mismatches between the human neck and trachea and the surrounding air.

The overall aim of our investigation was to establish a physically accurate model of light propagation in three-dimensions for the human neck, to be used for the forward problem in DOT. As the first step, our previous work has primarily developed the light propagation model in the human neck using two-dimensional time-dependent RTE [15]. For computational simplicity, the previous work has not considered the refractive-index mismatch at the trachea-tissue interface, although it is considered that the mismatch strongly influences on light propagation in the neck.

Although many works studying light propagation models in biological tissue for DOT have considered the refractive-index mismatch at the air-tissue interface (external boundary of the tissue), the mismatch at the void-tissue interface (inside the tissue) has been less treated. Arridge *et al.* have extensively investigated the effects of the mismatch at the void-tissue interface on light propagation in a turbid medium including a layered void region or a circular void region using MC simulations and the radiosity-diffusion model [16]. They have shown that the mismatch at the void-tissue interface weakly influences light propagation when the void region is a thin layer or the void region is located far from light source and detector positions. However, the trachea occupies a large cylindrical void region in the human neck, and light sources and detectors for DOT of the thyroid cancer are positioned near the trachea because the thyroid is located near the trachea. These conditions of the trachea and source-detector locations suggest strong effects of the mismatch at the trachea-tissue interface on light propagation.

This paper investigates three factors influencing light propagation in the human neck: (i) the presence of the trachea, (ii) reflection and refraction at the trachea boundary, and (iii) the effect of the neck organs other than the trachea.

The following section provides an explanation of the numerical methods based on the RTE. Section 3 provides the numerical results to investigate the three factors, and finally conclusions are detailed in section 4.

2. LIGHT PROPAGATION MODEL

2.1. Radiative transfer equation

Light propagation in turbid media such as biological tissue is accurately modeled by the RTE [17].

In two dimensions (2D), the RTE is given by

$$\begin{aligned} & \left[\frac{\partial}{v(\mathbf{r})\partial t} + \boldsymbol{\Omega} \cdot \nabla + \mu_a(\mathbf{r}) + \mu_s(\mathbf{r}) \right] I(\mathbf{r}, \boldsymbol{\Omega}, t) \\ & = \mu_s(\mathbf{r}) \int_{2\pi} d\boldsymbol{\Omega}' P(\mathbf{r}, \boldsymbol{\Omega} \cdot \boldsymbol{\Omega}') I(\mathbf{r}, \boldsymbol{\Omega}', t) + q(\mathbf{r}, \boldsymbol{\Omega}, t), \end{aligned} \quad (1)$$

where $I(\mathbf{r}, \boldsymbol{\Omega}, t)$ is in $\text{W cm}^{-1} \text{ rad}^{-1}$ and represents the intensity at one wavelength, which describes the photon energy flow as a function of the spatial location $\mathbf{r} = (x, y)$ in cm for a 2D Cartesian coordinate system, the angular direction $\boldsymbol{\Omega} = (\Omega_x, \Omega_y) = (\cos \theta, \sin \theta)$ ($\theta \in [0, 2\pi]$ in rad), and the time t in ps; $\mu_a(\mathbf{r})$ and $\mu_s(\mathbf{r})$ (in cm^{-1}) are the absorption and scattering coefficients, respectively, $v(\mathbf{r})$ is the speed of light in the turbid medium, $P(\mathbf{r}, \boldsymbol{\Omega} \cdot \boldsymbol{\Omega}')$ (in rad^{-1}) is the scattering phase function with $\boldsymbol{\Omega}'$ and $\boldsymbol{\Omega}$ denoting the incident and scattered directions, respectively, and $q(\mathbf{r}, \boldsymbol{\Omega}, t)$ (in $\text{W cm}^{-1} \text{ rad}^{-1}$) is a source function. For the formulation of $P(\mathbf{r}, \boldsymbol{\Omega} \cdot \boldsymbol{\Omega}')$, the 2D Henyey-Greenstein function [18, 19] is employed in this study,

$$P(\mathbf{r}, \boldsymbol{\Omega} \cdot \boldsymbol{\Omega}') = \frac{1}{2\pi} \frac{1 - [g(\mathbf{r})]^2}{1 + [g(\mathbf{r})]^2 - 2g(\mathbf{r})\boldsymbol{\Omega} \cdot \boldsymbol{\Omega}'} \quad (2)$$

with $g(\mathbf{r})$ being the anisotropic factor, $\int_{2\pi} d\boldsymbol{\Omega} (\boldsymbol{\Omega} \cdot \boldsymbol{\Omega}') P(\mathbf{r}, \boldsymbol{\Omega} \cdot \boldsymbol{\Omega}')$. Although there are several formulations of $q(\mathbf{r}, \boldsymbol{\Omega}, t)$ such as collimated incidence, here $q(\mathbf{r}, \boldsymbol{\Omega}, t)$ is given by an isotropic delta function, $\delta(t)\delta(\mathbf{r} - \mathbf{r}_s)$, with the source position at $\mathbf{r}_s = (x_s, y_s)$. This is because the dependence of the formulations on light propagation is sufficiently small when the detector is far from the source position. Here, the optical properties, μ_a , μ_s , v , and g , depend on the spatial location because they vary with organs in the human neck.

2.2. Refractive-index mismatched boundary condition

Reflection and refraction occur at the air-tissue interface due to the differences in the refractive indices. This leads to changes in the intensity and direction of the light reaching the air-tissue

interface. As shown in Fig. 1(a), the reflected and transmitted intensities of the light reaching the air-tissue interface from the tissue are given by

$$\begin{aligned} I(\mathbf{r}_b, \boldsymbol{\Omega}_{ref}, t) &= R(\boldsymbol{\Omega}_{in}, \boldsymbol{\Omega}_{out}; \mathbf{e}_n, n) I(\mathbf{r}_b, \boldsymbol{\Omega}_{in}, t), & \boldsymbol{\Omega}_{in} \cdot \mathbf{e}_n \geq 0 \\ I(\mathbf{r}_b, \boldsymbol{\Omega}_{out}, t) &= [1 - R(\boldsymbol{\Omega}_{in}, \boldsymbol{\Omega}_{out}; \mathbf{e}_n, n)] I(\mathbf{r}_b, \boldsymbol{\Omega}_{in}, t), \end{aligned} \quad (3)$$

where \mathbf{r}_b is the boundary position vector, $\boldsymbol{\Omega}_{in}$ is the direction of incidence, \mathbf{e}_n is the normal vector toward air, and n is the relative refractive index of the tissue; $\boldsymbol{\Omega}_{ref}$ and $\boldsymbol{\Omega}_{out}$ are the directions of reflection and refraction determined by Snell's law. The reflectivity R is calculated by Fresnel's law

$$R(\boldsymbol{\Omega}_{in}, \boldsymbol{\Omega}_{out}; \mathbf{e}_n, n) = \begin{cases} \frac{1}{2} \left[\frac{\sin^2(\theta_{out} - \theta_{in})}{\sin^2(\theta_{out} + \theta_{in})} + \frac{\tan^2(\theta_{out} - \theta_{in})}{\tan^2(\theta_{out} + \theta_{in})} \right], & 0 \leq \theta_{in} < \theta_c \\ 1, & \theta_c \leq \theta_{in} \leq \pi/2 \end{cases} \quad (4)$$

where $\theta_{in} = \cos^{-1}(\boldsymbol{\Omega}_{in} \cdot \mathbf{e}_n)$, $\theta_{out} = \cos^{-1}(\boldsymbol{\Omega}_{out} \cdot \mathbf{e}_n)$, and $\theta_c = \sin^{-1}(1/n)$. The critical angle, θ_c , is the angle of incidence above which the total internal reflection occurs. Reflection and refraction also occur at the void-tissue interface, and the reflected and transmitted intensities of the light reaching the interface from the tissue are given by Eqs. (3) and (4).

At the external air-tissue interface of the neck surface, $I(\mathbf{r}_b, \boldsymbol{\Omega}_{in}, t)$ is zero if $\boldsymbol{\Omega}_{in} \cdot \mathbf{e}_n < 0$, meaning non-reentry of light from the air [20]. At the internal air-tissue interface of the trachea (void region with air) inside the neck, the light from the void region can be either reflected or refracted at the interface, and reflected light can reenter into the tissue as shown in Fig. 1(b). Then, the reflected and transmitted intensities are given by

$$\begin{aligned} I(\mathbf{r}_b, \boldsymbol{\Omega}_{ref}, t) &= R(\boldsymbol{\Omega}_{in}, \boldsymbol{\Omega}_{out}; -\mathbf{e}_n, 1/n) I(\mathbf{r}_b, \boldsymbol{\Omega}_{in}, t), & \boldsymbol{\Omega}_{in} \cdot \mathbf{e}_n < 0 \\ I(\mathbf{r}_b, \boldsymbol{\Omega}_{out}, t) &= [1 - R(\boldsymbol{\Omega}_{in}, \boldsymbol{\Omega}_{out}; -\mathbf{e}_n, 1/n)] I(\mathbf{r}_b, \boldsymbol{\Omega}_{in}, t), \end{aligned} \quad (5)$$

where θ_c cannot be defined because the refractive index of the tissue is larger than that of air, meaning that there is no total reflection.

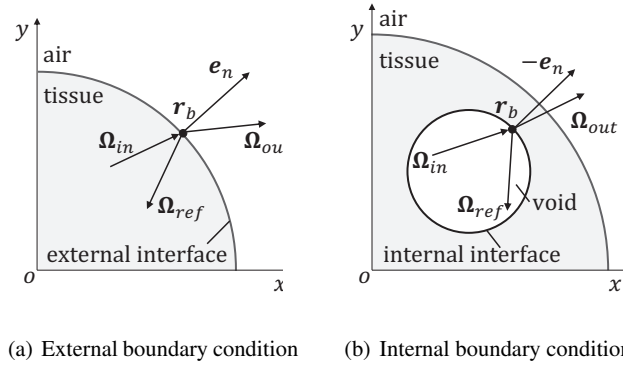


Figure 1. Refractive-index mismatches at air-tissue and void-tissue interfaces. \mathbf{r}_b is the boundary position vector; \mathbf{e}_n is the normal vector toward air; and Ω_{in} , Ω_{ref} , and Ω_{out} are the angular directions of incidence, reflection, and transmission, respectively.

3. NUMERICAL SCHEME

3.1. Finite-difference and discrete-ordinates methods

The RTE is numerically solved by using the finite-difference (FD) and discrete-ordinates (DO) methods. The independent variables, x , y , Ω_x , Ω_y , and t are discretized as $x_i = i\Delta x$ ($i \in \{1, 2, \dots, N_x\}$), $y_j = j\Delta y$ ($j \in \{1, 2, \dots, N_y\}$), $\Omega_{xk} = \cos \theta_k$, $\Omega_{yk} = \sin \theta_k$, $\theta_k = k\Delta\theta$ ($k \in \{1, 2, \dots, N_\theta\}$), and $t_m = m\Delta t$ ($m \in \{1, 2, \dots, N_t\}$), where Δx , Δy , $\Delta\theta$, and Δt are the constant step sizes, and N_x , N_y , N_θ , and N_t are the numbers of grid nodes and timesteps, respectively. In the discretized form, $I(\mathbf{r}, \boldsymbol{\Omega}, t)$ is expressed as $I_{ijk}^m = I(x_i, y_j, \Omega_{xk}, \Omega_{yk}, t_m)$, and $P(\mathbf{r}, \boldsymbol{\Omega} \cdot \boldsymbol{\Omega}')$ is as $P_{ijkk'} = P(x_i, y_j, \boldsymbol{\Omega}_k \cdot \boldsymbol{\Omega}_{k'}) \cdot \mu_s(\mathbf{r})$, $\mu_a(\mathbf{r})$, $g(\mathbf{r})$, and $v(\mathbf{r})$ are discretized and expressed in the same manner.

In the DO method, the scattering integral is reformulated as

$$\mu_s(\mathbf{r}) \int_{2\pi} d\boldsymbol{\Omega}' P(\mathbf{r}, \boldsymbol{\Omega} \cdot \boldsymbol{\Omega}') I(\mathbf{r}, \boldsymbol{\Omega}', t) = \mu_{s,ij} \sum_{k'=1}^{N_\theta} w_{k'} f_{k'} P_{ijkk'} I_{ijk'}^m + O(\Delta\theta^3), \quad (6)$$

where the weight, $w_{k'}$, to the direction, $\boldsymbol{\Omega}_{k'}$, is given as $2\pi/N_\theta$ based on the extended trapezoidal rule to satisfy the normalization of the scattering phase function ($\int_{2\pi} d\boldsymbol{\Omega}' P = 1$), and the renormalizing factor, $f_{k'}$, is given as $[\sum_{k=1}^{N_\theta} w_k P_{kk'}]^{-1}$ with a slight modification of the Liu's formulation [21] for fast convergence of the scattering integral. In the matrix notation, the scattering integral is expressed

as $\mathbf{P}\mathbf{I}^m$, where \mathbf{P} is a block diagonal matrix of size $N_x N_y N_\theta \times N_x N_y N_\theta$, and the vector \mathbf{I}^m is given as $(I_{000}^m, I_{001}^m, \dots, I_{ijk}^m, \dots, I_{N_x N_y N_\theta}^m)^T$ with T denoting transpose. For spatial discretization, we utilize the 3rd and 1st order upwind schemes (3UW and 1UW). Our previous study has shown that the 3UW is more accurate than the 1UW, and is able to reduce the computational loads in highly scattering media [15]. In non-scattering media (trachea), the 1UW is more suitable than the 3UW because the 3UW is slightly unstable and numerical oscillations appear at the early arriving time in non-scattering media. Based on the 3UW, the advection term in the x -axis is discretized as

$$\begin{aligned} & \Omega_x \partial I(\mathbf{r}, \boldsymbol{\Omega}, t) / \partial x \\ &= \begin{cases} \Omega_{xk} (6\Delta x)^{-1} [2I_{i+1jk}^m + 3I_{ijk}^m - 6I_{i-1jk}^m + I_{i-2jk}^m] + O(\Delta x^4) & \Omega_{xk} \geq 0 \\ \Omega_{xk} (6\Delta x)^{-1} [-I_{i+2jk}^m + 6I_{i+1jk}^m - 3I_{ijk}^m - 2I_{i-1jk}^m] + O(\Delta x^4) & \Omega_{xk} < 0 \end{cases} \end{aligned} \quad (7)$$

The advection term in the y -axis direction is discretized in the same manner as for the x -axis. For more details of the 1UW, refer to [22]. In the matrix notation, the advection term and linear terms (the second, third, and fourth terms on the left-hand side of Eq. (1)) are expressed as $\mathbf{A}\mathbf{I}^m$, where \mathbf{A} is a sparse matrix with the same size of \mathbf{P} .

For the temporal discretization, we employ the 3rd order TVD-Runge-Kutta method (3TVD-RK) [23], which is computationally efficient and stable than the 4th order Runge-Kutta method (4RK). Based on the 3TVD-RK, the discretized RTE is integrated with respect to t as

$$\mathbf{I}^{m+1} = \frac{1}{3} \mathbf{R} (\mathbf{I}^m + 2\mathbf{K}_2 + 2\mathbf{K}_3) + O(\Delta t^4), \quad (8)$$

where the matrix, \mathbf{R} , represents the reflectivity, and the coefficient vectors, \mathbf{K}_l ($l = 1, 2, 3$), are given by the following equations,

$$\begin{aligned} \mathbf{K}_1 &= \mathbf{I}^m + v\Delta t(-\mathbf{A} + \mathbf{P})\mathbf{I}^m, \\ \mathbf{K}_2 &= \frac{3}{4}\mathbf{I}^m + \frac{1}{4}\mathbf{K}_1 + \frac{1}{4}v\Delta t(-\mathbf{A} + \mathbf{P})\mathbf{K}_1, \\ \mathbf{K}_3 &= v\Delta t(-\mathbf{A} + \mathbf{P})\mathbf{K}_2. \end{aligned} \quad (9)$$

A preliminary study has shown that the 3TVD-RK can reduce computational time by about 25 percent of that for 4RK because two vectors, \mathbf{K}_l ($l = 1, 2$), are allocated in the computer memory for the 3TVD-RK during runtime, while for the 4RK, four vectors, \mathbf{K}_l ($l = 1, 2, 3, 4$), must be allocated.

3.2. Anatomical human neck model

We developed an anatomical human neck model by utilizing MR images of a human neck (adult woman) as shown in Fig. 2(a). We performed segmentation of the MR image and extracted the organs of the human neck: the trachea, spine, spinal cord, and blood vessels, as shown in Fig. 2(b). Other organs such as muscle, bone, and adipose tissue were combined into homogeneous background tissue. The thyroid gland was included in the background tissue, although it anatomically wraps around the trachea. The curved geometries of the organs and background tissue in the image were mapped with regular grids. The segmentation procedure has been primarily developed in the previous work [15].

The optical properties of the organs and background tissue in the near-infrared wavelength of about 800 nm are listed in Table I, referring to [9, 24]. The values of the properties vary widely with the kinds of tissue, suggesting that appropriate numerical schemes vary with the different kinds of tissue. The background tissue, spine, and spinal cord are highly scattering media ($\mu_s \gg \mu_a$, $\mu_a < 1 \text{ cm}^{-1}$), and therefore the 3UW is used inside these. The trachea, meanwhile, is almost all non-scattering and non-absorbing medium ($\mu_s \ll 1 \text{ cm}^{-1}$, $\mu_a \ll 1 \text{ cm}^{-1}$), and the 1UW is used inside the trachea. Numerical calculations of the light propagation in the blood vessels is the most difficult because μ_s and μ_a of the blood vessels are very large and g is very close to unity, resulting in very heavy computational loads (especially for increasing N_θ). A preliminary study has shown that numerical results of the RTE for the blood vessels are accurate when N_θ is larger than approximately 120 resulting in a much larger memory requirement. In this study, instead of the RTE, the delta-Eddington approximation (dEA) is employed for numerical calculations of light propagation in the blood vessels. The dEA decomposes the forward-peaked scattering into delta-function and isotropic

scattering components to reduce the computational loads [25, 26], and the scattering phase function, $P(\mathbf{r}, \boldsymbol{\Omega} \cdot \boldsymbol{\Omega}')$, is reduced to $g(\mathbf{r})\delta(1 - \boldsymbol{\Omega} \cdot \boldsymbol{\Omega}') + 1 - g(\mathbf{r})$. It has been reported that the dEA holds better for media with g very close to unity [20] corresponding to an extremely highly forward-peaked scattering. By employing the dEA, N_θ is reduced to 100 without a loss of accuracy of numerical solutions. In the background and neck organs, other than the trachea and blood vessels, g is homogeneously given as 0.9 which is less close to unity than that for the blood vessels but still indicating a highly forward-peaked scattering. Thus, in the background and neck organs, N_θ is given as 100 to obtain accurate solutions of the RTE.

From Table I, it is suggested that the DA can also be employed for the background tissue and organs other than the trachea and blood vessels because the tissues are highly scattering media. However, the DA is invalid in the regions of trachea and blood vessels and their vicinities. In addition, the DA is inaccurate in the spatial region with source-detector distances shorter than $\rho_{DA} \sim 10/\mu'_t$ and in the temporal region earlier than $t_{DA} \sim 10/v\mu'_t$ after the pulse input, where $\mu'_t = \mu_a + \mu_s(1 - g)$ [27]. In the case of the background tissue, for example, ρ_{DA} and t_{DA} are given by 1.2 cm and 56.2 ps. Hence, the use of the DA for the whole region of the human neck and whole time period is impossible, and if one wants to use the DA, the hybrid model of the RTE and DA [27] is necessary with evaluating a spatial and temporal regime for the DA to be valid.

The refractive-index mismatched boundary conditions are incorporated at the air-tissue and trachea-tissue interfaces while in the previous work [15], the boundary condition at the trachea-tissue interface was not considered. At the air-tissue interface, a part of the scattered light from the tissue is reflected back to the tissue, and the remaining part goes out into the open air. Once light goes out to the open air, it is assumed that the light will never come back to the tissue. At the trachea-tissue interface, a part of the scattered light from the tissue is reflected back to the tissue, and the remaining part is transmitted to the trachea. The transmitted light travels straight inside the trachea, and reaches another position on the interface. Then, the light is reflected back to the trachea or transmitted to the background tissue. As a result, it is likely that large differences in

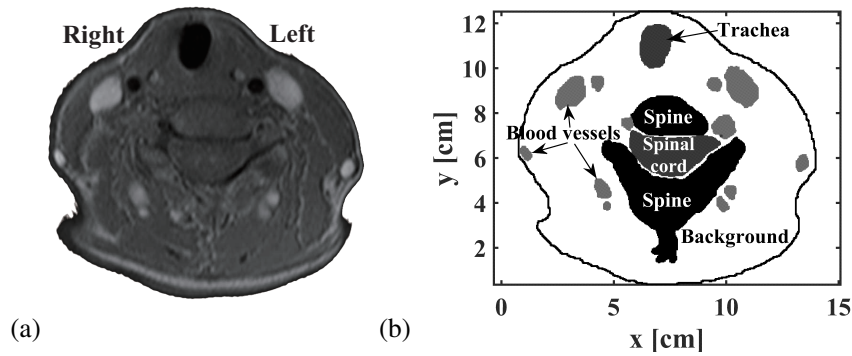


Figure 2. (a) Transverse MR image of the human neck, (b) neck organs after the segmentation. Light gray regions represent the blood vessels.

Table I. Optical properties of the neck organs and background tissue in the anatomical human neck model at the wavelength of about 800 nm [9, 24]

	$\mu_a[\text{cm}^{-1}]$	$\mu_s[\text{cm}^{-1}]$	g	n
Background tissue	0.30	80.0	0.9	1.4
Trachea (void)	0.0001	0.0001	0.0	1.0
Spine	0.25	148	0.9	1.4
Spinal cord	0.17	882	0.9	1.4
Blood vessels	4.76	675	0.992	1.4

light propagation are observed around the trachea for models with and without the refractive-index mismatch.

Other than the trachea, the organs are assumed to have a constant value of the refractive index, $n = 1.4$, meaning that neither reflection nor refraction take places at the interfaces between different organs in the background tissue.

3.3. Level set method

To incorporate the refractive-index mismatched boundary condition at the curved boundaries and interfaces, it is necessary to assign boundary nodes, r_b , and calculate the normal vectors, e_n , at

these boundary nodes. In this study, we perform this process using the level set method, which has been widely used for capturing moving boundaries of objects in imaging problems [28, 29]. There are many ways of implementing the level set method with various degrees of accuracy and efficiency, and here we adopt one that is simple and efficient. In the later section, we will show that this level set method is appropriately implemented in the numerical calculations of light propagation in the human neck.

In the level set method, the signed distance function, $\varphi(\mathbf{r})$, is the commonest choice as the level set function,

$$\varphi(\mathbf{r}) = \begin{cases} -dist(\mathbf{r}) < 0 & \mathbf{r} \in S_{in} \\ dist(\mathbf{r}) > 0 & \mathbf{r} \in S_{out} \end{cases}, \quad (10)$$

where \mathbf{r} is a position on a regular grid, $dist(\mathbf{r})$ is the distance between \mathbf{r} and the curved boundary, S_{in} and S_{out} are domains inside and outside the curved boundary, respectively, as shown in Fig. 3(a). A boundary node, \mathbf{r}_b , is assigned in S_{in} where the sign of $\varphi(\mathbf{r})$ for the boundary node is different from that for its nearest neighbor node. A normal vector, \mathbf{e}_n , is calculated by $\nabla\varphi(\mathbf{r})/|\nabla\varphi(\mathbf{r})|$ based on the central difference method.

Figure 3(b) shows the level set method as applied to the external boundary of the human neck, which is implicitly represented by $\varphi(\mathbf{r}) = 0$, and \mathbf{r}_b and \mathbf{e}_n are calculated. Because $\varphi(\mathbf{r})$ is calculated from the grid points with the spatial step size Δx , $\varphi(\mathbf{r})$ is discretized with Δx . This makes the results for \mathbf{e}_n in Fig. 3(b) discrete. In addition to the external boundary, the level set method is applied to the trachea boundary.

3.4. Step sizes in discretization

Throughout the paper, the constant step sizes are selected as $\Delta x = \Delta y = 0.02$ cm, $\Delta\theta = 0.0628$ rad ($N_\theta = 100$), and $\Delta t = 0.04$ ps. These step size values were determined in our preliminary study, in which it has been confirmed that the numerical solutions of the RTE agree very well with analytical solutions to the RTE in infinite homogeneous media having optical properties of neck organs. The total number of the square grids with the side of 0.02 cm is approximately 3×10^5 .

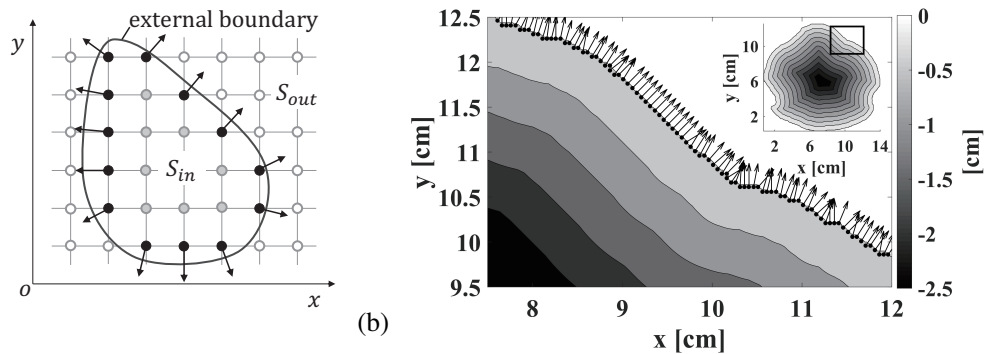


Figure 3. (a) Schematic of the level set method: a solid curve represents an external boundary of the object, solid black circles boundary nodes, $\mathbf{r}_b \in S_{in}$, and arrows the outward normal vectors, e_n . Open and gray circles represent the exterior and interior nodes of the object, respectively; (b) Contour of the signed distance function, $\varphi(\mathbf{r})$, for the external boundary of the human neck in the enlarged view (a region enclosed by a rectangle in the whole view of the human neck as the inset). e_n and \mathbf{r}_b are plotted in the figure with a rough spatial step size $\Delta x = 0.05$ cm for easy visualization.

The source code for the numerical calculations are written in the C programming language, and for numerical efficiency, all the matrices are compressed to vectors as the compressed row storage format. Also, parallel CPU programming is implemented with a 24 thread computer (Intel Xeon X5690 @3.47GHz) by using the OpenMP, which is a portable and shared-memory programming scheme.

The average computation time using the RTE for the time period up to 1000 ps is 3219 min. Although we can reduce the computational time further by using rough step sizes, this study focuses on investigation for light propagation in the human neck rather than that of computational efficiency. It is confirmed that by decreasing N_θ from 100 to 48, the computation time is reduced to one-fifth of that at $N_\theta = 100$ while the numerical errors increase by a few percent. Also, a multi-thread computer will help in reducing the computation time further because our code is suitable for parallel computing.

Our numerical scheme for solving the RTE was validated by the analytical solutions of the RTE [27, 15] and DA. At a region in a finite medium far from the boundaries, the numerical solutions of the RTE can be compared with the analytical solutions of the RTE in an infinite medium. The results

have shown that the numerical solutions of the RTE at the region far from the boundaries agree with the analytical solutions of the RTE [27, 15]. At the curved boundaries of the medium, the numerical scheme can be validated by the analytical solution of the DA in a circular medium. The Appendix confirms the validity of the numerical scheme at the curved boundaries by the analytical solution of the DA.

3.5. Measurement quantities and conditions

As the measurable quantities, we consider the outward flux, J^+ , at the external boundary of the human neck, and the fluence rate, Φ , inside the human neck. The formulations of J^+ and Φ are given as

$$J^+(\mathbf{r}_b, t) = \int_{\Omega \cdot \mathbf{e}_n > 0} d\Omega (\Omega \cdot \mathbf{e}_n) I(\mathbf{r}_b, \Omega, t), \quad \Phi(\mathbf{r}, t) = \int_{2\pi} d\Omega I(\mathbf{r}, \Omega, t). \quad (11)$$

A light source is incident on the front center surface of the human neck at the position $(x, y) = (7.38 \text{ cm}, 12.52 \text{ cm})$, shown as a red arrow in Fig. 4. The assumption of the point source matches the actual measurement using an optical fiber with a core diameter of 0.005 cm, which is much smaller than the spatial step size of 0.02 cm in computation. Here, we consider eight detectors located at the front of the neck surface, R1:(6.38 cm, 12.52 cm), R2:(5.38 cm, 12.2 cm), R3:(4.38 cm, 11.2 cm), R4:(3.38 cm, 10.42 cm), L1:(8.38 cm, 12.24 cm), L2:(9.38 cm, 11.46 cm), L3:(10.38 cm, 10.64 cm), and L4:(11.38 cm, 10.22 cm), respectively. The detectors have a sensing diameter of 0.5 cm, so the results of J^+ are averaged over the spatial regions of the detectors. The reason for these source and detector locations is that the locations are near the location of the thyroid gland, aiming for a high sensitivity in a diagnosis of thyroid cancer.

As listed in Table II, four numerical models A, B, C, and D are considered to investigate the effects on light propagation of the presence of the trachea, of the refractive-index mismatch at the trachea boundary, and of the locations of the other organs inside the neck. Although Model B is based on the primarily developed model [15], Models A, C, and D are developed here.

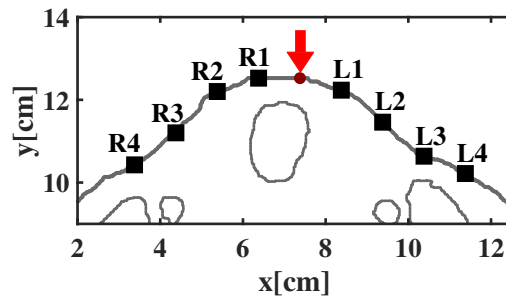


Figure 4. Positions of the source and detectors at the front surface of the human neck; the source position (red circle) is at $(x, y) = (7.38 \text{ cm}, 12.52 \text{ cm})$, and the detector positions (solid squares) are at R1:(6.38 cm, 12.52 cm), R2:(5.38 cm, 12.2 cm), R3:(4.38 cm, 11.2 cm), R4:(3.38 cm, 10.42 cm), L1:(8.38 cm, 12.24 cm), L2:(9.38 cm, 11.46 cm), L3:(10.38 cm, 10.64 cm), and L4:(11.38 cm, 10.22 cm), respectively.

Table II. Numerical models for investigating light propagation in the human neck

Model	Medium	Refractive index in the trachea
A	Background tissue	-
B	Background tissue+trachea	1.4 (match)
C	Background tissue+trachea	1.0 (mismatch)
D	Background tissue+trachea +surrounding organs	1.0 (mismatch)

4. RESULTS

4.1. Influence of the trachea

In this subsection, we investigate the influences of the presence of the trachea and the refractive-index mismatch at the trachea-tissue interface on light propagation in the human neck by comparing three models, Model A: a homogeneous medium consisting of the background tissue without the trachea; Model B: a heterogeneous medium consisting of the background tissue and the trachea (background tissue+trachea medium) under the refractive-index matched boundary condition at

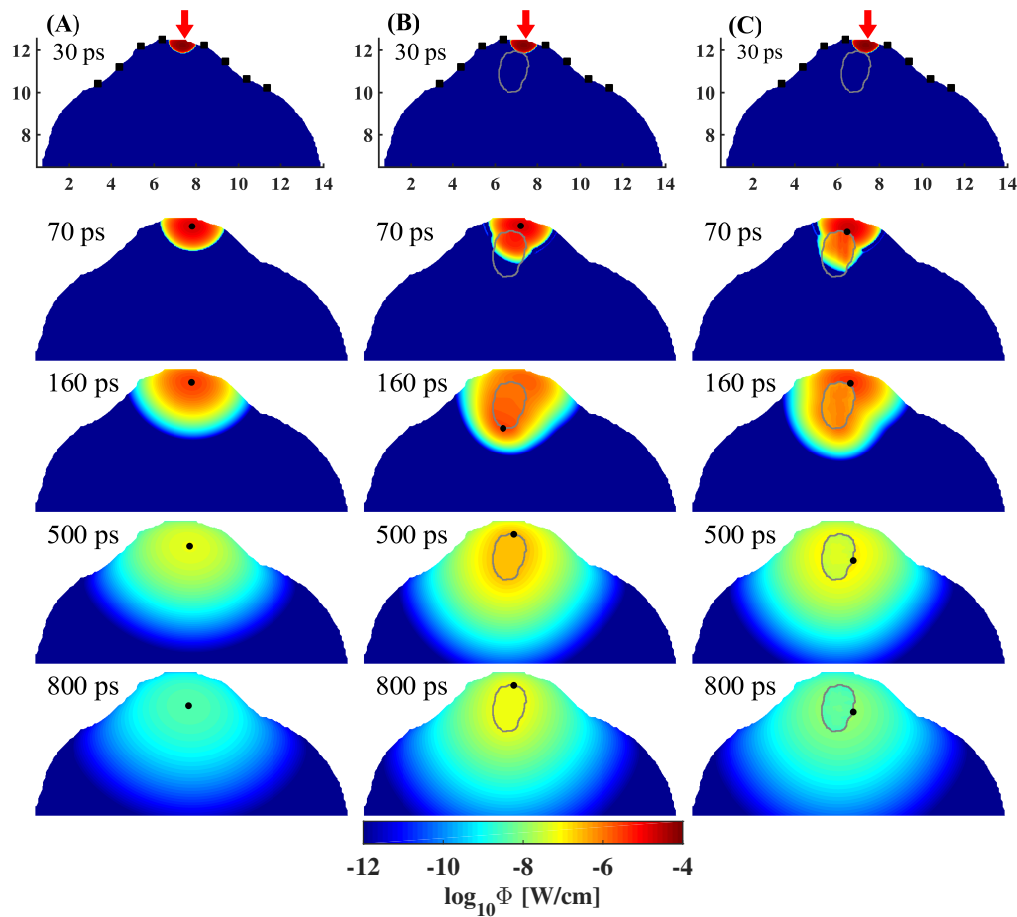


Figure 5. Spatial distributions of Φ in logarithmic scale, calculated from the RTE for the three models in Table II, Model A (left column): homogeneous medium; Model B (middle column): refractive-index match at the trachea-tissue interface; and Model C (right column): refractive-index mismatch at the trachea-tissue interface. In the subfigures at $t = 30$ ps (top row), the plot ranges of the x - y coordinates [cm] are shown, light sources are represented by red arrows, and detector locations are represented by solid squares. In the subfigures in the middle and right columns, the boundaries of the trachea (trachea-tissue interfaces) are denoted by gray solid curves, and the positions of the maximum Φ are represented by solid dots. The figures are snapshots from Video 1 for Model A, Video 2 for Model B and Video 3 for Model C found online. Note that only the region of interest is shown while computation was performed for the whole region of Fig. 2.

the trachea-tissue interface by setting n as 1.4 in the trachea; and Model C: the background tissue+trachea medium incorporating the refractive-index mismatch at the trachea-tissue interface with $n = 1.0$ in the trachea.

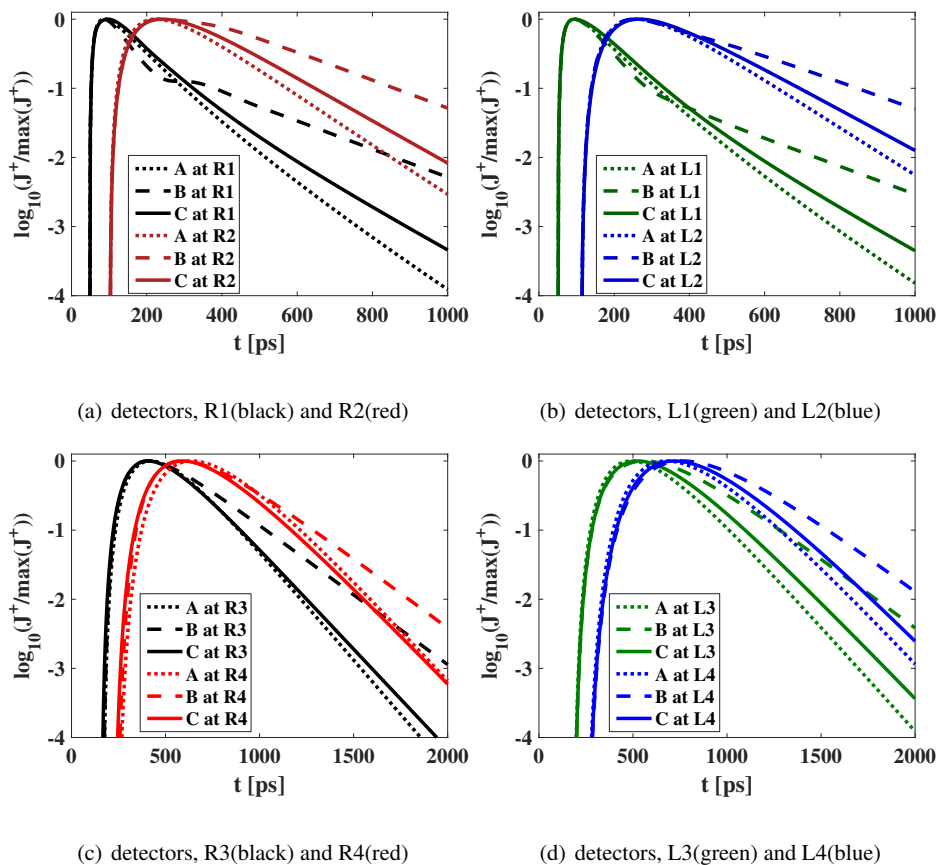


Figure 6. Time-resolved profiles of J^+ at the eight detectors, R1 to R4, and L1 to L4, for Model A to Model C. Source-detector locations are shown in Fig. 4.

Figure 5 shows the spatial distributions of Φ , in logarithmic scale, calculated from the RTE at set times in the homogeneous background medium for Model A in the left column; and in the background+trachea medium for Model B with the refractive-index match and Model C with the refractive-index mismatch in the middle and right columns, respectively, when the light source is placed on the front center surface of the human neck at the position $(x, y) = (7.38 \text{ cm}, 12.52 \text{ cm})$ (top row, Fig. 5). There are clear differences between the three models after light reaches the trachea boundary ($t > 30 \text{ ps}$).

At $t = 70 \text{ ps}$ (second row from the top, Fig. 5), the front of the light propagation is strongly influenced by the models. For Model A, the front spreads circularly, while for Models B and C, the fronts are irregular early in the model calculations due to the presence of the trachea. The front

for Model B moves faster than that for Model A because no scattering takes place in the trachea. Moreover, the front for Model C moves even faster than that in Model B because the speed of the light, v , for Model C is higher than that of Model B.

At $t = 160$ ps, for Model C, a smaller amount of light propagates into the trachea than with Model B because when light in the background reaches the trachea-tissue interface, reflection to the background dominates transmission to the trachea. Also, for Model C the light reaching the trachea-tissue interface from the trachea is largely transmitted into the background compared with reflection of the light.

At longer times ($t = 500$ and 800 ps), the light attenuation is different for the three models. Light attenuation with Model A is larger than with Models B and C due to the absence of the trachea, where neither scattering nor absorption takes place. Also light attenuation with Model C is larger than with Model B; as with Model C the refractive-index mismatch suppresses light propagation into the trachea, resulting in increases in the light attenuation in the background. For Model B, a larger amount of light goes into the trachea, resulting in less light attenuation in the background at the later times.

The positions of the maximum Φ , r_Φ , are indicated by black dots in the subfigures. In addition to the subfigures, trajectory animations of r_Φ are shown in three linked videos (Video 1, Video 2, and Video 3) for the three models. With Model A, r_Φ moves less inward in the medium than with Models B and C due to the light attenuation in the background at $t \lesssim 500$ ps. With Model B, r_Φ moves back and forth between the deep and shallow sides of the trachea boundary, as shown in the subfigures at 160, 500, and 800 ps (see also Video 2). This movement is caused by the diffusive reflection at the trachea-tissue interface as will be explained in the following. Light reaching the trachea-tissue interface from the trachea is scattered in all directions, and a part of the scattered light returns to the trachea. This kind of reflection, termed the diffusive reflection, repeats inside the trachea. With Model C, r_Φ moves along the trachea boundary in the background due to reflection from the background, and refraction from the trachea.

Now, we will discuss the influences of the outward flux measured at the front of the neck surface, J^+ . The time-resolved profiles of J^+ at the eight detectors, R1 to R4 and L1 to L4, are plotted in Fig. 6. As shown in Fig. 6(a), the profiles at R1 and R2 in the rising periods ($t < t_{peak}$ with the peak at t_{peak}) are very similar for the three models, meaning that light reaching at R1 and R2 in the early periods has propagated through a region near the neck surface without being affected by the trachea. In the decay periods ($t > t_{peak}$), the profiles vary with the models. The profiles for Model A in the decay periods are sharper than those for Models B and C, meaning that light decays faster with Model A. This is because the trachea suppresses the light attenuation as detailed above. The profiles with Model C are sharper than those with Model B, suggesting that the component reflected to the front surface from the region around the trachea due to the refractive-index mismatch at the trachea boundary is smaller than the component due to the diffusive reflection.

As shown in Fig. 4, the geometries of the human neck surface and the trachea boundary are asymmetric with respect to the line parallel to the y -axis passing through the source position ($x = 7.38$ cm). The effects of the asymmetry on the light propagation can be evaluated by comparing the profiles at R1 and R2 with those at L1 and L2. In Fig. 6(b) the profiles at L1 and L2 show the same tendency as the profiles at R1 and R2, suggesting that the effects of the asymmetry are small for the detectors close to the source.

The profiles at the detectors far from the source and trachea are plotted in Figs. 6(c) and (d), and here the profiles are different for the three models, showing that the trachea affects light propagation also in the regions far from the source and trachea. This may be ascribed to the source location near the trachea, suggesting the conclusion that light propagation in a wide region at and around the trachea is influenced by the trachea.

The results in Fig. 6 suggest that the measurements of light at the human neck surface are strongly influenced by the trachea, and that numerical calculations have to incorporate the refractive-index mismatch at the trachea-tissue interface. Otherwise, estimates of the spatial distributions of the optical properties by the inverse processes in DOT will deviate considerably from the true values.

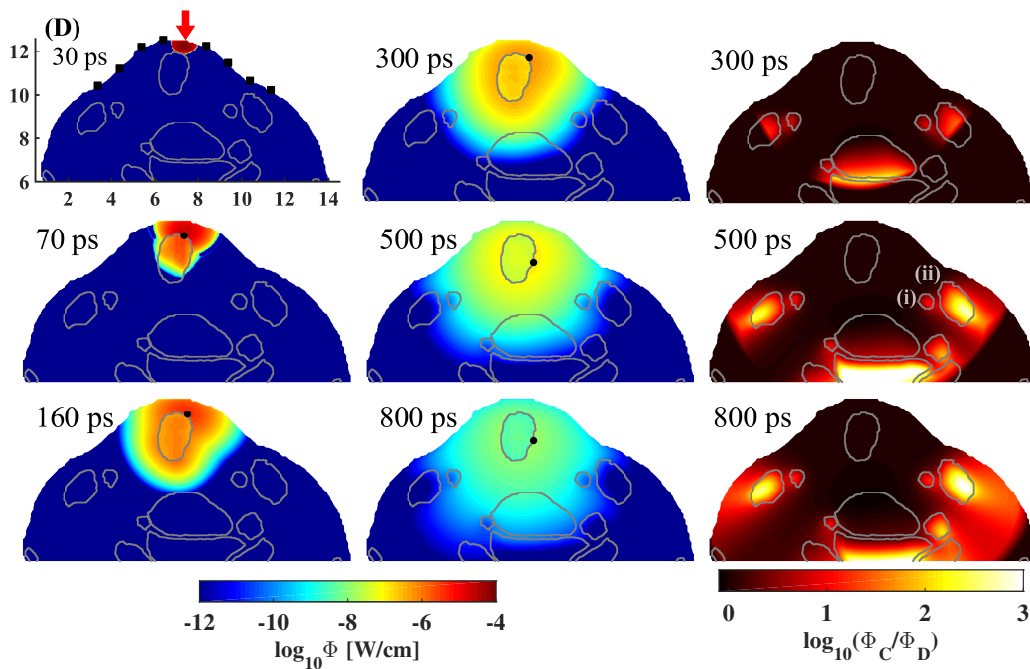


Figure 7. (Left and middle columns) spatial distributions of Φ in logarithmic scale at specified times for Model D using the RTE. The boundaries of the neck organs are denoted by the gray enclosed areas. (Right column) the logarithmic differences in Φ between Model C and Model D, $\log_{10}(\Phi_C/\Phi_D)$, at the late times of 300, 500 and 800 ps. Examples of small and large blood vessels are indicated in the subfigure at the time of 500 ps by (i) and (ii), respectively. Other details are the same as in Fig. 5.

4.2. Influences of neck organs other than the trachea

In this subsection, we investigate the influence of the presence of neck organs other than the trachea (spine, spinal cord, and blood vessels) on the light propagation by comparing two models; Model C: the trachea+background tissue, and Model D: the human neck model. In the two models, we incorporate the refractive-index mismatched boundary condition at the trachea as listed in Table. II.

The spatial distributions of Φ for Model D are plotted in the left and middle columns of Fig. 7 for the times from 30 ps to 800 ps. Up to the time of $t = 160$ ps, the distributions in the two models (Model C [shown in Fig. 5] and Model D) are quite similar. In the later time period from 300 ps to 800 ps, differences in the distributions between the two models appear around the neck organs. To make the differences clear, logarithmic differences in Φ between Model C and Model D,

$\log_{10}(\Phi_C/\Phi_D)$, are plotted in the right column of Fig. 7. Regions around the neck organs except for the trachea have positive values of the differences, meaning that the local light attenuation around them is larger for Model D than for Model C. The positive values at the region around the spine are smaller compared with those around the spinal cord and blood vessels, because the differences in the optical properties between the spine and the background tissue are smaller than those between the spinal cord or blood vessels and the background tissue, as listed in Table I. Also, the positive values depend on the size of the neck organs; in the regions of small blood vessels and their vicinities (indicated by (i) in the subfigure at the time of 500 ps in the right column, for example) the positive values are smaller than those in the regions of large blood vessels and their vicinities (like indicated by (ii) in the subfigure). The reason is probably that light penetrates through the small blood vessels before it is exposed to much interaction with the small blood vessels.

Figure 8 compares the temporal profiles of J^+ and the maximum values at the detectors on the left of the source, L1 to L4, for Models C and D. It was observed (not shown here) that the profiles at the detectors on the right of the source, R1 to R4, show the same tendency as those on the left of the source. As shown in Figs. 8(a) and (c), the profiles and the maximum values for Model D agree well with those of Model C at L1 and L2 near the source and far from the large blood vessels, suggesting that the temporal profiles measured near the source and far from the large blood vessels are insensitive to the presence of neck organs other than the trachea inside the human neck. As shown in Figs. 8(b) and (c), the profiles and the maximum values of the two models are different at L3 and L4, far from the source and near the large blood vessel (indicated as (ii) in Fig. 7). At L3, the profile for Model D decays faster and the maximum value of the profile is slightly smaller than that for Model C, although the peak times are very similar for the two models. The changes in the profile are more prominent at L4 which is closer to the large blood vessel than L3. At L4, the peak with Model D appears earlier, it decays faster, and the maximum value is much smaller than with Model C. In general, when the absorption coefficient of a homogeneous medium increases in time-resolved measurements, the peak of J^+ shifts to earlier times and the maximum value of J^+ decreases. This would suggest J^+ measured near absorbing objects in a heterogeneous medium also shows peaks

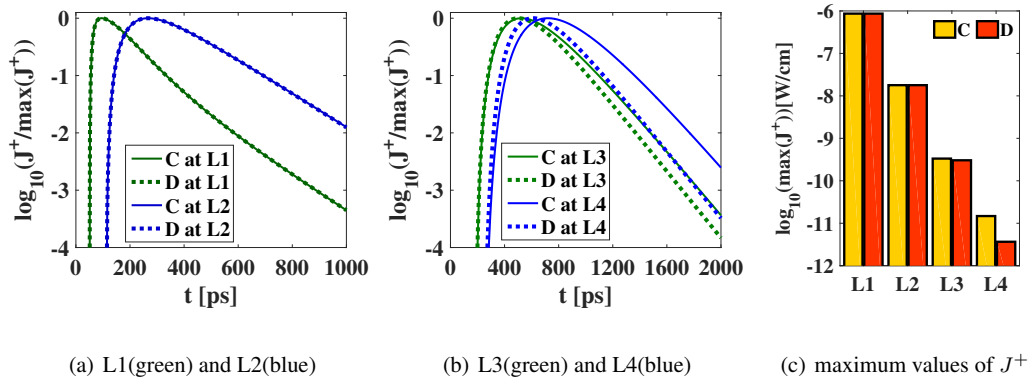


Figure 8. Time-resolved profiles of J^+ at the detectors on the left of the source, (a) L1 and L2, and (b) L3, and L4, for Models C and D. (c) Maximum values of J^+ [W/cm] at the detectors, L1 to L4, for the two models.

earlier and reach smaller maximum values than when no absorbing objects are present. The results in Figs. 8(b) and (c) are consistent with the above results. Nevertheless, the effects of the other neck organs are quite small because the maximum value of J^+ at L4 is five orders of magnitude smaller than that at L1 as shown in Fig. 8(c). These results suggest the possibility of modeling the other neck organs simply as a background medium as long as the source and detectors are far from large blood vessels.

5. CONCLUSIONS

To develop a physically accurate model of light propagation in the human neck to be used for the forward problem in DOT, we have investigated the influence of three factors on light propagation in the human neck, numerically, by 2D time-dependent RTE: (i) the presence of the trachea, (ii) the refractive-index mismatch at the trachea-tissue interface, and (iii) the effect of neck organs other than the trachea such as the spine, spinal cord, blood vessels.

The results here showed that the presence of the trachea and the refractive-index mismatch at the trachea boundary strongly influence light propagation in the human neck and light fluxes measured

at the front of the neck surface. Also that other neck organs than the trachea influence the light propagation very weakly when source and detectors are far from the large blood vessels.

APPENDIX: VALIDATION OF THE NUMERICAL SCHEME INCLUDING CURVED BOUNDARIES

To validate the numerical scheme for calculating light propagation in a turbid medium including curved boundaries, a comparison of numerical results using the RTE and the analytical solutions will be described here. Because no analytical solution of the RTE with curved boundaries has been reported, we utilized the analytical solution of the DA for a 2D homogeneous circular medium with a radius R (Fig. A1(a)). Research has shown that in scattering media the DA is valid in regions far from the source position and in periods of time long after the source injection [30, 27]. The analytical solution of the DA for the outward flux, J^+ , in a circular medium under an extrapolated boundary condition is given as Eq. (A1), by referring to [31, 32]:

$$\begin{aligned}
 J^+(R, \alpha, t; r_0, R') &= -\frac{vD}{\pi R'^2} \exp(-\mu_a vt) \\
 &\times \sum_{m=-M}^M \cos(m\alpha) \sum_{\beta_m}^B \exp(-vD\beta_m^2 t) \frac{\beta_m J'_m(\beta_m R) J_m(\beta_m r_0)}{[J'_m(\beta_m R')]^2},
 \end{aligned}
 \tag{A1}$$

where the source and detector positions are denoted as $(r_0, 0)$ and (R, α) in polar coordinates, respectively, as shown in Fig. A1(a). Here, r_0 is given by $R - [\mu'_s]^{-1}$, and $R' = R + \gamma(n)D$ is the extrapolated radius with a coefficient $\gamma(n)$ as a function of n and the diffusion coefficient $D = [2\mu'_s]^{-1}$, $\beta_m \in \mathbb{R}$ are positive roots of $J_m(\beta_m R') = 0$, where J_m is the m -th order Bessel function of the first kind ($m \in \mathbb{N}$), and J'_m is the derivative of J_m with respect to the radius, and M and B are the numbers of the summations which are theoretically infinite.

For a comparison of Eq. (A1) with the numerical results for the RTE, we consider a homogeneous circular medium with $R = 2.0$ cm and the optical properties given as those of the spine listed in Table 1. Equation (A1) is numerically computed with $M = B = 50$, and $\gamma = 2.83$ in the case of

$n = 1.4$. We have confirmed that even if M and B are larger than 50, the solutions of Eq. (A1) change only little.

Figure A1(b) shows the computed time-resolved profiles of J^+ using the RTE and Eq. (A1) at the source-detector angle of $\alpha = \pi/3$, and π . The numerical results calculated using the RTE agree well with Eq. (A1), around the peak at t_{peak} (320 ps for $\alpha = \pi/3$; 800 ps for $\alpha = \pi$) and the decay period ($t > t_{peak}$). At the rising period ($t < t_{peak}$), there are small differences in J^+ between the two. This is because the DA assumes infinity for the speed of light while the speed is finite in the RTE [33], and the difference is clearer with larger μ_a [15]. The results in Fig. A1 confirm the validity of our numerical scheme for the case including curved boundaries. We have also confirmed the validity for other cases of optical properties (for the background tissue and spinal cord).

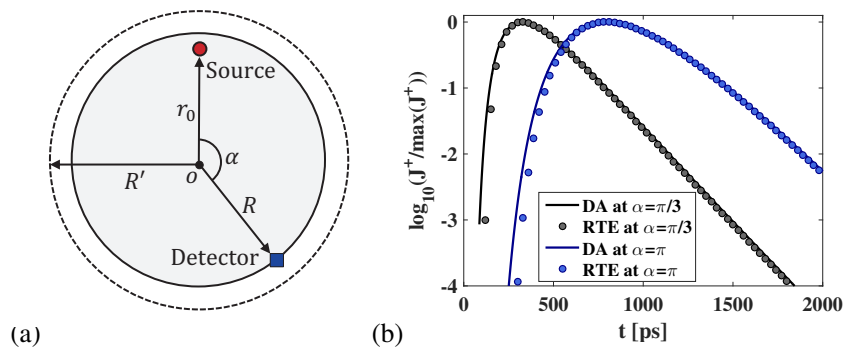


Figure A1. (a) Homogeneous circular medium with radius R . Source and detector are represented by a red dot and blue square, respectively, and the angle between the source and detector positions is α . An isotropic light impulse is incident in the medium at a distance from the surface of $[\mu'_s]^{-1} = R - r_0$, and R' represents the radius of the extrapolated boundary (dashed circle); (b) Logarithmic time-resolved profiles of J^+ for the RTE and DA in the circular medium, normalized by the peak values. Black and blue represent the profiles at $\alpha = \pi/3$ and π , respectively.

ACKNOWLEDGEMENTS

We wish to express appreciation to Y. Tatekura, K. Hattori, and E. Miyakawa for technical support. We are also grateful to Dr. S. Okawa, Dr. E. Okada, Dr. K. Hashimoto, Dr. H. Kawaguchi, Dr. Y. Tanikawa and Dr. G. Nishimura for helpful discussions and insightful comments. This work was supported by JSPS

KAKENHI Grant Numbers 15K17980, 25287028, and 15K06125, and by the Japan Agency for Medical Research and Development.

REFERENCES

1. MCHENRY RC, PHITAYAKORN R. Follicular Adenoma and Carcinoma of the Thyroid Gland. *The Oncologist* 2011; **16**:585–593.
2. Arridge SR. Optical tomography in medical imaging. *Inverse Problems* 1999; **15**(2):R41–R93.
3. Gibson AP, Hebden JC, Arridge SR. Recent advances in diffuse optical imaging. *Physics in Medicine and Biology* 2005; **50**(4):R1–R43.
4. Wang, Z G and Sun, L Z and Fajardo, L L and Wang G. Modeling and reconstruction of diffuse optical tomography using adjoint method. *Communications Numerical Methods in Engineering* 2009; **25**:657–665.
5. Yamada Y, Okawa S. Diffuse Optical Tomography : Present Status and Its Future. *Optical Review* 2014; **21**(3):185–205.
6. Hielscher AH, Klose AD, Scheel AK, Moa-Anderson B, Backhaus M, Netz U, Beuthan J. Sagittal laser optical tomography for imaging of rheumatoid finger joints. *Physics in Medicine and Biology* 2004; **49**(7):1147–1163.
7. Klose AD, Pöschinger T. Excitation-resolved fluorescence tomography with simplified spherical harmonics equations. *Physics in Medicine and Biology* 2011; **56**(5):1443–1469.
8. Okawa S, Hoshi Y, Yamada Y. Improvement of image quality of time-domain diffuse optical tomography with l_p sparsity regularization. *Biomedical Optical Express* 2011; **2**(12):3334–3348.
9. Dehaes M, Gagnon L, Vignaud A, Valabr R, Grebe R, Wallois F, Benali H. Quantitative investigation of the effect of the extra-cerebral vasculature in diffuse optical imaging : a simulation study. *Biomedical Optical Express* 2011; **2**(3):680–695.
10. Kannan, R and Przekwas A. A computational model to detect and quantify a primary blast lung injury using near-infrared optical tomography. *International Journal for Numerical Methods In Biomedical Engineering* 2011; **27**:13–28.
11. Kannan, R and Przekwas A. A near-infrared spectroscopy computational model for cerebral hemodynamics. *International Journal for Numerical Methods In Biomedical Engineering* 2012; **28**:1093–1106.
12. Sultan, E and Pourrezaei, K and Ghandjbakhche, A and Daryoush A. 3D Numerical modeling and its experimental verifications for an inhomogeneous head phantom using broadband fNIR system. *International Journal for Numerical Methods in Biomedical Engineering* 2014; **30**:353–364.
13. Hielscher AH, Alcouffe RE, Barbour RL. Comparison of finite-difference transport and diffusion calculations for photon migration in homogeneous and heterogeneous tissues. *Physics in Medicine and Biology* 1998; **43**:1285–1302.

14. Fang Q. Mesh-based Monte Carlo method using fast ray-tracing in Plücker coordinates. *Biomedical optics express* 2010; **1**(1):165–75.
15. Fujii H, Okawa S, Nadamoto K, Okada E, Yamada Y, Hoshi Y, Watanabe M. Numerical modeling of photon migration in human neck based on the radiative transport equation. *Journal of Applied Nonlinear Dynamics* 2016; **5**(1):117–125 eprint arXiv:1603.03769 [physics.med-ph].
16. Arridge SR, Dehghani H, Schweiger M, Okada E. The finite element model for the propagation of light in scattering media: a direct method for domains with nonscattering regions. *Medical Physics* 2000; **27**:252–264.
17. Chandrasekhar S. *Radiative Transfer*. Dover: New York, 1960.
18. Henyey LG, Greenstein LJ. Diffuse radiation in the galaxy. *Journal of Astrophysics* 1941; **93**:70–83.
19. Heino J, Arridge S, Sikora J, Somersalo E. Anisotropic effects in highly scattering media. *Physical Review E* 2003; **68**:031 908 1–8.
20. Klose AD, Ntziachristos V, Hielscher AH. The inverse source problem based on the radiative transfer equation in optical molecular imaging. *Journal of Computational Physics* 2005; **202**(1):323–345.
21. Liu L, Ruan L, Tan H. On the discrete ordinates method for radiative heat transfer in anisotropically scattering media. *International Journal of Heat and Mass Transfer* 2002; **45**(15):3259–3262.
22. Klose AD, Netz U, Beuthan J, Hielscher AH. Optical tomography using the time-independent equation of radiative transfer — Part 1 : forward model. *Journal of Quantitative Spectroscopy & Radiative Transfer* 2002; **72**:691–713.
23. Gottlieb S, Shu CW. Total variation diminishing Runge-Kutta schemes. *Mathematics of Computation* 1998; **67**(221):73–85.
24. Bashkatov AN, Genina EA, Tuchin VV. OPTICAL PROPERTIES OF SKIN , SUBCUTANEOUS , AND MUSCLE TISSUES : A REVIEW. *Journal of Innovative Optical Health Sciences* 2011; **4**(1):9–38.
25. Joseph JH, Wiscombe WJ, Weinman JA. The delta-Eddington approximation for radioactive flux transfer. *Journal of Atmospheric Sciences* 1976; **33**:2452–2459.
26. Welch A, van Gemert M. *Optical-Thermal Response of Laser-Irradiated Tissue*. Plenum Press, London, 1995.
27. Fujii H, Okawa S, Yamada Y, Hoshi Y. Hybrid model of light propagation in random media based on the time-dependent radiative transfer and diffusion equations. *Journal of Quantitative Spectroscopy & Radiative Transfer* 2014; **147**:145–154.
28. Osher S, Fedkiw RP. Level Set Methods: An Overview and Some Recent Results. *Journal of Computational Physics* 2001; **169**(2):463–502.
29. Adalsteinsson D, Sethian JA. A Fast Level Set Method for Propagating Interfaces. *Journal of Computational Physics* 1995; **118**(2):269–277.
30. Yoo KM, Liu F, Alfano RR. When does the diffusion approximation fail to describe photon transport in random media? *Physical Review Letter* 1990; **64**(22):2647–2650.
31. Arridge SR, Cope M, Delpy DT. The theoretical basis for the determination of optical pathlengths in tissue : temporal and frequency analysis. *Physics in Medicine and Biology* 1992; **37**(7):1531–1560.

32. Sassaroli A, Martelli F, Zaccanti G, Yamada Y. Performance of fitting procedures in curved geometry for retrieval of the optical properties of tissue from time-resolved measurements. *Applied Optics* 2001; **40**(1):185–197.
33. Guo Z, Kumar S. Discrete-ordinates solution of short-pulsed laser transport in two-dimensional turbid media. *Applied Optics* 2001; **40**(19):3156–3163.